International Journal of Engineering Science 47 (2009) 1–20

Contents lists available at ScienceDirect

International Journal of Engineering Science

journal homepage: www.elsevier.com/locate/ijengsci

Elastic cylinder with helicoidal orthotropy: Theory and applications

S. Leelavanichkul [a], A. Cherkaev [b,*]

[a] Department of Mechanical Engineering, University of Utah, United States
[b] Department of Mathematics, University of Utah, 155 S 1400 E, Salt Lake City, Utah 84112, United States

ARTICLE INFO

Article history:
Received 17 June 2008
Accepted 17 June 2008
Available online 30 October 2008

Keywords:
Anisotropic elasticity
Laminated cylinder
Helicoidal orthotropy
Spiralling grains
Biomechanics
Structural optimization

ABSTRACT

The elasticity equations are derived for a helicoidally symmetric cylinder. An isotropic cylinder in the center is wrapped by a thick layer of a material with helicoidal anisotropy formed by spiraling of fibers around the core. Such structures are seen in springs, armored cables, trusses, composites, and biostructures. Structure under axial loading and pure bending are considered. The analytical expressions for displacements are obtained from equations of three-dimensional elasticity. The results are verified numerically via the finite element method. The stiffness matrix for an equivalent simplified model that links the displacements of the ends with the applied force and momentum is formulated. A coupling effect is revealed: the bar twists and elongates when axially loaded.

The developed technique is used to explain an evolution of structure in nature. A pine trunk with spiralling grain is investigated from an optimization of a mechanical construction viewpoint. We model the trunk as an anisotropic cylinder with helicoidal symmetry and compute the displacements and stresses using nonlinear finite element model. An optimized spiralling angle of the grains accounts for a composite failure, transverse deflection, and fluid transportation. We suggest a combined criterion that could explain this spiralling morphology.

1. Introduction

We study a long elastic cylinder that consist of isotropic core and a cylindrical layer. The layer has a helicoidal symmetry: The orthotropic material in the shell spirals around a core. Solving the problem we quantitatively describe the coupling of elongation and twisting due to the helicoidal anisotropy. The structure can be used as a mechanism that transforms these types of motion between one another. This effect is emphasized in a simplified link model that we present.

Helicoidal structures are met in armored cables, trusses, ropes, composites (Fig. 1). Fiber-reinforced composite materials with helicoidal symmetry (laminated cylinders) are also often seen in aircraft landing gear, a bridge column, or a bicycle frame. In composites, the more rigid filaments in a bundle can be achieved by the use of the spiralling reinforced filling compound. In cables, the spiraling allows for a combination of strength and flexibility in bending. The interest in helixes has grown in the recent years after the discovery of nanocoils [1] that are promising components of designs.

Furthermore, a special area of applications of helicoidal cylinders are biostructures, where the spiralling geometry is widely observed. A micro level, protein structures form helixes. At macro level, these are found in bones, sea sponges, narwhal tooth, among other examples, (Fig. 2). The spiralling of the fiber in a tree's trunk was investigated earlier in our paper [2]. One wonders what the evolutionary significance of such design is. We expect that there must be a good evolutionary reason for a natural design to becomes more complex.

* Corresponding author.
E-mail addresses: sleelava@eng.utah.edu (S. Leelavanichkul), cherk@math.utah.edu (A. Cherkaev).

0020-7225/$ - see front matter
doi:10.1016/j.ijengsci.2008.06.017

Fig. 1. Examples of structures with spirals in engineering design.

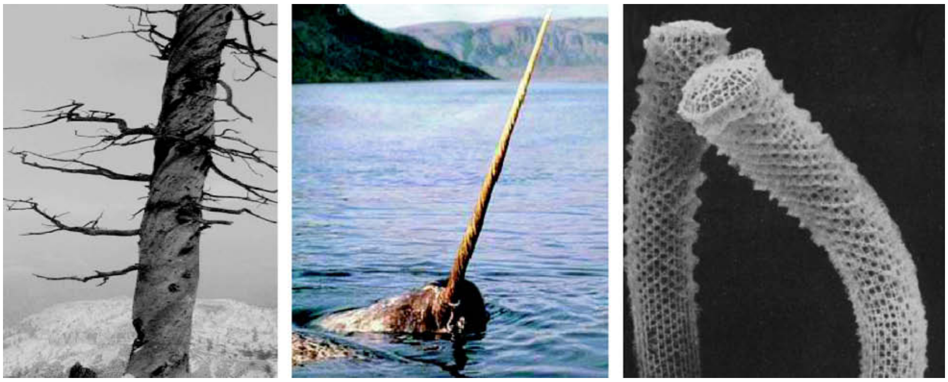

Fig. 2. Ponderosa Pine (left); Narwhal whale (center); Sea sponge (right).

Given the broad region of applications of helicoidal structures, it is surprising that we were not able to find papers that explicitly solve the elasticity problem for a cylinder with helicoidal symmetry. This paper aims to work out the solution to it by revisiting the classical work of Lekhnitskii [3,4]. The theory of laminated shells [5] gives a satisfactory approximation for a thin-walled cylinder, but not for a thick helicoidal orthotropic layer. Particularly, our approach, based on three-dimensional elasticity, allows for calculation of radial stress component, and the dependence of the stress tensor on the radius can be tracked. Here, we generalize the classical approach of Lekhnitskii [3,4] and Pagano [6] which analyze the three-dimensional elasticity equations. Lekhnitskii's solution describes the stress potential for a cylinder with cylindrical anisotropy ($\phi = 0$). Here, we consider a general case and we find the formulas for the displacement vector. The exposition generally follows [7].

The structure of the paper is as following. In Section 2, the problem is stated. The elasticity equations, structural boundary conditions, and the transformation of the coordinates systems according to the spiralling angle of orthotropy are discussed. Section 3 presents the general solution for the cylinder under axial loading and pure bending. The closed-form analytical solution is obtained by using the displacement potentials approach. Section 4 illustrates a computational example of a cylinder made of aluminum 6061-T6 wrapped by T300/862 graphite/epoxy. In Sections 5 and 6, the developments of the equivalent one-dimensional link model and its application in finite element formulation are discussed, respectively.

The developed technique is used to investigate the significances of the spiraling grains of trees. In Section 7 we explain the rationale of the modelling. Assumptions, design criteria, and numerical setup are given in Sections 8 and 9. We consider multiple criteria in order to determine advantages and disadvantages of spiraling morphologies and quantitatively justify the "optimal pitch angle" of the helix. Our analysis is an example of "inverse optimization", which defines optimality criteria that match the observed structure. In Section 10 we describe the findings.

2. Modelling

2.1. Elasticity equations

We consider a three-dimensional axisymmetric model of the cylinder, assuming that the angle ϕ of spiraling is constant. The cylinder is either elongated, twisted, or bent. The effective stiffness of the structure, the pointwise stress tensor and the

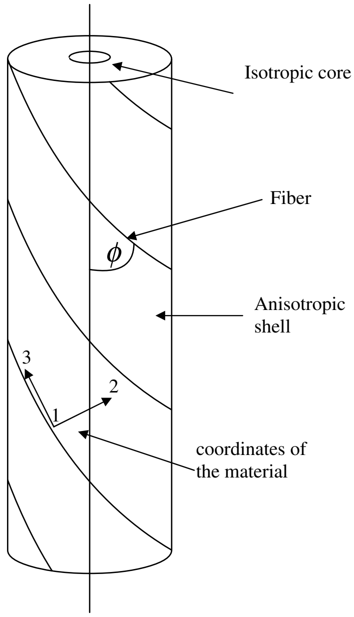

Fig. 3. A cylindrical isotropic object that is wrapped with a single layer of thick shell having its fiber oriented at an arbitrary angle.

displacement vector, are determined using three-dimensional elasticity coupled with assumptions based on helicoidal symmetry. Our goal is to find an analytic solution to the problem or direct calculation of the equivalent stiffness and the displacement components.

The system of differential equations of helicoidally symmetric elasticity permits the separation of variables and leads to differential equations for radius-dependent displacement components. They are derived similarly to Lekhnitskii [3,4]. The presented results allows for explicit calculation of the effective elastic moduli and local stresses for all angles of the spiralling. This technique is conveniently used for the optimization of the spiralling angle.

The solution to the displacement field also allows us to formulate an equivalent one-dimensional model of a cylinder with an inner helix. The cylinder shows a coupling effect, twisting and elongating when axially loaded.

Consider an infinite cylinder of the radius R made of an orthotropic linear elastic material with the compliance $\mathbf{S}$ loaded by bending moment M, and the axial load P. We want to compute the stress tensor $\boldsymbol{\sigma}$ and trace its dependence on the orientation of the orthotropy. Assume that stresses inside the cylinder satisfy equations of linear elasticity. In the absence of body forces, the equilibrium equations,

$$\nabla \cdot \boldsymbol{\sigma} = 0, \tag{1}$$

in cylindrical coordinates (r,θ,z) have the form

$$\begin{aligned} 0 &= \frac{1}{r}\frac{\partial}{\partial r}(r\sigma_{rr}) + \frac{1}{r}\frac{\partial}{\partial \theta}\sigma_{r\theta} + \frac{\partial}{\partial z}\sigma_{rz} - \frac{\sigma_{\theta\theta}}{r}, \\ 0 &= \frac{1}{r^2}\frac{\partial}{\partial r}(r^2\sigma_{\theta r}) + \frac{1}{r}\frac{\partial}{\partial \theta}\sigma_{\theta\theta} + \frac{\partial}{\partial z}\sigma_{\theta z}, \\ 0 &= \frac{1}{r}\frac{\partial}{\partial r}(r\sigma_{zr}) + \frac{1}{r}\frac{\partial}{\partial \theta}\sigma_{z\theta} + \frac{\partial}{\partial z}\sigma_{zz}, \end{aligned} \tag{2}$$

where σ_{rr}, $\sigma_{\theta\theta}$, σ_{zz}, $\sigma_{\theta z}$, σ_{zr}, and $\sigma_{r\theta}$ are the components of the stress tensor.

The strain–displacement relations in cylindrical coordinates are

$$\begin{aligned} &\varepsilon_{rr} = \frac{\partial u_r}{\partial r}, \quad \varepsilon_{\theta\theta} = \frac{1}{r}\frac{\partial u_\theta}{\partial \theta} + \frac{u_r}{r}, \quad \varepsilon_{zz} = \frac{\partial u_z}{\partial z}, \quad \varepsilon_{\theta z} = \frac{1}{2}\left(\frac{\partial u_\theta}{\partial z} + \frac{1}{r}\frac{\partial u_z}{\partial \theta}\right), \\ &\varepsilon_{zr} = \frac{1}{2}\left(\frac{\partial u_z}{\partial r} + \frac{\partial u_r}{\partial z}\right), \quad \varepsilon_{r\theta} = \frac{1}{2}\left(\frac{1}{r}\frac{\partial u_r}{\partial \theta} + \frac{\partial u_\theta}{\partial r} - \frac{u_\theta}{r}\right). \end{aligned} \tag{3}$$

Here, ε_{rr}, $\varepsilon_{\theta\theta}$, ε_{zz}, $\varepsilon_{\theta z}$, ε_{zr}, and $\varepsilon_{r\theta}$ are the components of the strain tensor ε. The relationship between stresses and strains in an anisotropic material is expressed through generalized Hooke's law:

$$\boldsymbol{\varepsilon} = \mathbf{S} : \boldsymbol{\sigma} \text{ or } \boldsymbol{\sigma} = \mathbf{C} : \boldsymbol{\varepsilon}, \tag{4}$$

where $\mathbf{S}$ and $\mathbf{C} = (\mathbf{S})^{-1}$ are the fourth order tensors of compliance and its inverse, stiffness, respectively. The component form of this relation is $\boldsymbol{\varepsilon}_{ij} = \mathbf{S}_{ijkl}\boldsymbol{\sigma}_{kl}$ and $\boldsymbol{\sigma}_{ij} = \mathbf{C}_{ijkl}\colon \boldsymbol{\varepsilon}_{kl}$.

2.2. Boundary conditions

The boundary conditions are prescribed such that the outer surface of the shell is free of stresses. It is assumed that there is no slip at the interface between the core and the shell:

$$\begin{aligned}
&\sigma_r|_{r_1} = \sigma_r|_{r_2}, \quad \tau_{\theta z}|_{r_1} = \tau_{\theta z}|_{r_2},\\
&\tau_{rz}|_{r_1} = \tau_{rz}|_{r_2}, \quad \tau_{r\theta}|_{r_1} = \tau_{r\theta}|_{r_2},\\
&u(r,\theta)|_{r_1} = u(r,\theta)|_{r_2}, \quad v(r,\theta)|_{r_1} = v(r,\theta)|_{r_2}, \quad w(r,\theta)|_{r_1} = w(r,\theta)|_{r_2}
\end{aligned} \tag{5}$$

Here r_1 is the inner radius and r_2 is the outer radius of the shell. The end conditions are solved separately for each loading scenarios.

Axial loading:

$$\int_0^{r_2}\int_0^{2\pi} \sigma_{zz_{\text{iso}}} r\mathrm{d}r + \int_{r_1}^{r_2}\int_0^{2\pi} \sigma_{zz_{\text{aniso}}} r\mathrm{d}r = P, \tag{6}$$

$$\int_0^{r_2}\int_0^{2\pi} \sigma_{\theta z_{\text{iso}}} r^2\mathrm{d}r + \int_{r_1}^{r_2}\int_0^{2\pi} \sigma_{\theta z_{\text{aniso}}} r^2\mathrm{d}r = 0, \tag{7}$$

Pure bending:

$$\int_0^{2\pi}\int_0^{r_1} \sigma_{zz_{\text{iso}}} r^2 \sin\theta \mathrm{d}r\mathrm{d}\theta + \int_0^{2\pi}\int_{r_1}^{r_2} \sigma_{zz_{\text{aniso}}} r^2 \sin\theta \mathrm{d}r\mathrm{d}\theta = M, \tag{8}$$

$$\int_0^{2\pi}\int_0^{r_1} \sigma_{zz_{\text{iso}}} r^2 \cos\theta \mathrm{d}r\mathrm{d}\theta + \int_0^{2\pi}\int_{r_1}^{r_2} \sigma_{zz_{\text{aniso}}} r^2 \cos\theta \mathrm{d}r\mathrm{d}\theta = 0. \tag{9}$$

where r_1 and r_2 are the inner and outer radius of the anisotropic shell, respectively. The only nonhomogeneous boundary condition Eqs. (6) and (8) provide the scaling of the loads.

2.3. Coordinates transformation

Assume that the material is orthotropic and consider a differential element of a helicoidally anisotropic cylinder. Tensor **S** of the compliance is characterized by an orthogonal triplet of *material coordinates* ($\mathbf{e}_1$, $\mathbf{e}_2$, $\mathbf{e}_3$). In these coordinates, the generalized Hooke's law has the form:

$$\begin{Bmatrix} \epsilon_{11}^* \\ \epsilon_{22}^* \\ \epsilon_{33}^* \\ \epsilon_{23}^* \\ \epsilon_{13}^* \\ \epsilon_{12}^* \end{Bmatrix} = \begin{bmatrix} \frac{1}{E_{11}} & -\frac{v_{21}}{E_{22}} & -\frac{v_{31}}{E_{33}} & 0 & 0 & 0 \\ -\frac{v_{12}}{E_{11}} & \frac{1}{E_{22}} & -\frac{v_{32}}{E_{33}} & 0 & 0 & 0 \\ -\frac{v_{13}}{E_{11}} & -\frac{v_{23}}{E_{22}} & \frac{1}{E_{33}} & 0 & 0 & 0 \\ 0 & 0 & 0 & \frac{1}{G_{23}} & 0 & 0 \\ 0 & 0 & 0 & 0 & \frac{1}{G_{13}} & 0 \\ 0 & 0 & 0 & 0 & 0 & \frac{1}{G_{12}} \end{bmatrix} \begin{Bmatrix} \sigma_{11}^* \\ \sigma_{22}^* \\ \sigma_{33}^* \\ \sigma_{23}^* \\ \sigma_{13}^* \\ \sigma_{12}^* \end{Bmatrix}. \tag{10}$$

The considered bar possesses cylindrical anisotropy as shown in Fig. 4. Hence, it is desirable that the analysis is carried out in cylindrical coordinates.

We need to transform the Hooke's law from the material coordinates ($\mathbf{e}_1$, $\mathbf{e}_2$, $\mathbf{e}_3$) to cylindrical coordinates ($\mathbf{e}_r$, $\mathbf{e}_\theta$, $\mathbf{e}_z$). The material coordinates are related to cylindrical coordinates through a rotation of angle ϕ about the radial axis. The transformation of coordinate is as follows:

$$\mathbf{e}_r = \mathbf{e}_1, \tag{11}$$

$$\begin{aligned}
&\mathbf{e}_\theta = \cos\phi\mathbf{e}_2 + \sin\phi\mathbf{e}_3,\\
&\mathbf{e}_z = -\sin\phi\mathbf{e}_2 + \cos\phi\mathbf{e}_3.
\end{aligned} \tag{12}$$

The rotation matrix Ω is written according to (12) as

$$\mathbf{\Omega} = \begin{bmatrix} 1 & 0 & 0 \\ 0 & \cos\phi & \sin\phi \\ 0 & -\sin\phi & \cos\phi \end{bmatrix}. \tag{13}$$

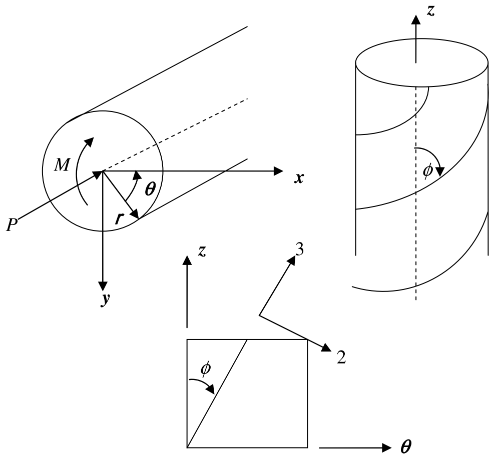

Fig. 4. Coordinate systems.

The stress and strain tensors are transformed according to

$$\boldsymbol{\sigma} = \mathbf{K}\boldsymbol{\sigma}^* \quad \text{and} \quad \boldsymbol{\varepsilon} = (\mathbf{K}^{-1})^{\mathrm{T}}\boldsymbol{\varepsilon}^*, \tag{14}$$

where tensor product $\mathbf{K} = \boldsymbol{\Omega} \otimes \boldsymbol{\Omega}$ is the fourth order rotation tensor ($K_{ijkl} = \Omega_{ij}\Omega_{kl}$). The transformed compliance matrix can be written as

$$\mathbf{S} = \left(\mathbf{K}^{-1}\right)^{\mathrm{T}} \mathbf{S}^* \mathbf{K}^{-1}, \tag{15}$$

where $\mathbf{S}^*$ is the compliance matrix in the material coordinates. The compliance and stiffness matrices, $\mathbf{S}$ and $\mathbf{C}$, have the following forms:

$$\mathbf{S} = \begin{bmatrix} a_{11} & a_{12} & a_{13} & a_{14} & 0 & 0 \\ a_{21} & a_{22} & a_{23} & a_{24} & 0 & 0 \\ a_{31} & a_{32} & a_{33} & a_{34} & 0 & 0 \\ a_{41} & a_{42} & a_{43} & a_{44} & 0 & 0 \\ 0 & 0 & 0 & 0 & a_{55} & a_{56} \\ 0 & 0 & 0 & 0 & a_{65} & a_{66} \end{bmatrix} \quad \text{and} \quad \mathbf{C} = \begin{bmatrix} c_{11} & c_{12} & c_{13} & c_{14} & 0 & 0 \\ c_{21} & c_{22} & c_{23} & c_{24} & 0 & 0 \\ c_{31} & c_{32} & c_{33} & c_{34} & 0 & 0 \\ c_{41} & c_{42} & c_{43} & c_{44} & 0 & 0 \\ 0 & 0 & 0 & 0 & c_{55} & c_{56} \\ 0 & 0 & 0 & 0 & c_{65} & c_{66}, \end{bmatrix}.$$

where a_{ij} and c_{ij} are the non-zero rotated elements. After the coordinates transformation, the compliance and stiffness matrices have 20 non-zero components. They are computed through the material properties (12 components) and an angle ϕ.

3. Solution by displacement potentials

Consider an elastic equilibrium of a loaded homogeneous cylinder having a cylindrical anisotropy. Because the quantities a_{i4} and c_{i4} ($i = 1,2,3,4$) are not zero, there are no planes of elastic symmetry normal to the generators of the cylinder. Therefore, the cross sections do not remain plane after deformation.

Here we neglect rigid body motion, and assume that the cylinder is infinitely long. These assumptions imply that the strain components are independent of z and can be expressed as

$$\varepsilon(r,\theta) = \varepsilon_0(r) + \varepsilon_1(r)\cos\theta + \varepsilon_2(r)\sin\theta. \tag{16}$$

Following Lekhnitskii [4], we introduce a relation D as

$$D = a_{13}\sigma_{rr} + a_{23}\sigma_{\theta\theta} + a_{33}\sigma_{zz} + a_{34}\sigma_{\theta z}, \tag{17}$$

and express stress along the generator, σ_{zz},

$$\sigma_{zz} = \frac{D}{a_{33}} - \frac{1}{a_{33}}(a_{13}\sigma_{rr} + a_{23}\sigma_{\theta\theta} + a_{34}\sigma_{\theta z}). \tag{18}$$

From Eq. (16), Hooke's law becomes

$$\frac{\partial u_r}{\partial r} = \beta_{11}\sigma_{rr} + \beta_{12}\sigma_{\theta\theta} + \beta_{14}\sigma_{\theta z} + \frac{a_{13}}{a_{33}}D, \tag{19}$$

$$\frac{1}{r}\frac{\partial u_\theta}{\partial \theta} + \frac{u_r}{r} = \beta_{21}\sigma_{rr} + \beta_{22}\sigma_{\theta\theta} + \beta_{24}\sigma_{\theta z} + \frac{a_{23}}{a_{33}}D, \tag{20}$$

$$\frac{\partial u_z}{\partial z} = D, \tag{21}$$

$$\frac{\partial u_\theta}{\partial z} + \frac{1}{r}\frac{\partial u_z}{\partial \theta} = \beta_{41}\sigma_{rr} + \beta_{42}\sigma_{\theta\theta} + \beta_{44}\sigma_{\theta z} + \frac{a_{43}}{a_{33}}D, \tag{22}$$

$$\frac{\partial u_z}{\partial r} + \frac{\partial u_r}{\partial z} = a_{55}\sigma_{rz} + a_{56}\sigma_{r\theta}, \tag{23}$$

$$\frac{1}{r}\frac{\partial u_r}{\partial \theta} + \frac{\partial u_\theta}{\partial r} - \frac{u_\theta}{r} = a_{65}\sigma_{rz} + a_{66}\sigma_{r\theta}, \tag{24}$$

where $\beta_{ij} = a_{ij} - \frac{a_{i3}a_{j3}}{a_{33}}$ are the reduced strain coefficients [4]. Integration of Eqs. (21)–(23) leads to

$$\begin{aligned} u_z &= Dz + W(r,\theta), \\ u_\theta &= z\left(\beta_{41}\sigma_{rr} + \beta_{42}\sigma_{\theta\theta} + \beta_{44}\sigma_{r\theta} + \frac{a_{43}}{a_{33}}D\right) - \frac{1}{r}\left(\frac{z^2}{2}\frac{\partial D}{\partial \theta} + z\frac{\partial W(r,\theta)}{\partial \theta}\right) + V(r,\theta), \\ u_r &= z(a_{55}\sigma_{rz} + a_{56}\sigma_{r\theta}) - \left(\frac{z^2}{2}\frac{\partial D}{\partial r} + z\frac{\partial W(r,\theta)}{\partial r}\right) + U(r,\theta). \end{aligned} \tag{25}$$

Substituting these displacements into Eqs. (19)–(24), and equating the coefficients of z and z^2 on the left and right, D is computed as

$$D = Ar\cos\theta + Br\sin\theta + C. \tag{26}$$

The independent of z terms are expressed as

$$\frac{\partial U(r,\theta)}{\partial r} = \beta_{11}\sigma_{rr} + \beta_{12}\sigma_{\theta\theta} + \beta_{14}\sigma_{\theta z} + \frac{a_{13}}{a_{33}}D, \tag{27}$$

$$\frac{1}{r}\frac{\partial V(r,\theta)}{\partial \theta} + \frac{U(r,\theta)}{r} = \beta_{21}\sigma_{rr} + \beta_{22}\sigma_{\theta\theta} + \beta_{24}\sigma_{\theta z} + \frac{a_{23}}{a_{33}}D, \tag{28}$$

$$\frac{1}{r}\frac{\partial U(r,\theta)}{\partial \theta} + \frac{\partial V(r,\theta)}{\partial r} - \frac{U(r,\theta)}{r} = a_{65}\sigma_{rz} + a_{66}\sigma_{r\theta}, \tag{29}$$

$$\frac{1}{r}\frac{\partial W(r,\theta)}{\partial \theta} = \beta_{41}\sigma_{rr} + \beta_{42}\sigma_{\theta\theta} + \beta_{44}\sigma_{\theta z} + \frac{a_{43}}{a_{33}}D + \vartheta r, \tag{30}$$

$$\frac{\partial W(r,\theta)}{\partial r} = a_{55}\sigma_{rz} + a_{56}\sigma_{r\theta}. \tag{31}$$

Utilizing Eqs. (31) and (30), Eq. (25) is rewritten as

$$u = U(r,\theta) - \frac{z^2}{2}(A\cos\theta + B\sin\theta), \tag{32}$$

$$v = V(r,\theta) - \frac{z^2}{2}(B\cos\theta - A\sin\theta) + \vartheta rz, \tag{33}$$

$$w = W(r,\theta) - z(Ar\cos\theta + Br\sin\theta + C). \tag{34}$$

Next, the solution to $U(r,\theta)$, $V(r,\theta)$, and $W(r,\theta)$ are sought in the form of:

$$U(r,\theta) = r^\alpha(U_A\sin n\theta + U_B\cos n\theta) \tag{35}$$

$$V(r,\theta) = r^\alpha(V_A\sin n\theta + V_B\cos n\theta) \tag{36}$$

$$W(r,\theta) = r^\alpha(W_A\sin n\theta + W_B\cos n\theta). \tag{37}$$

Here, U_A, V_A, W_A, U_B, V_B and W_B are constants and α is the root of the characteristic equation of the corresponding system of ordinary differential equations. For our goals, only two terms $n = 0, n = 1$ are relevant. The first term, $n = 0$, corresponds to the axial loading. In this case, the displacement is independent of θ and z. The second term, $n = 1$, corresponds to the bending. We treat these two cases separately. The unknown constants are determined from the boundary conditions shown in Section 2.2.

Next, we look at two separate load cases, axial loading, and pure bending. The objective is to determine the displacement potential, $U(r, \theta)$, $V(r, \theta)$, $W(r, \theta)$, for each case.

3.1. Displacements under axial loading

Recall that the model consists of an isotropic core and helicoidal anisotropic shell. For the solid isotropic core, the displacements are uncoupled and can be solved independently from the differential equations. In the case of an axial loading, Eqs. (32)–(34) become

$$u = U(r), \quad v = V(r) + \vartheta rz, \quad w = W(r) + Cz. \tag{38}$$

Substituting the above expression into the equilibrium equations, the following are found

$$U(r) = \frac{C_1^2 r + C_2}{r}, \quad V(r) = \frac{C_3^2 r + C_4}{r}, \quad W(r) = C_5 + C_6 \ln r. \tag{39}$$

The solution is regular at the center ($r_1 = 0$), therefore, $C_2 = C_4 = C_6 = 0$. Because there is no rigid body movement, we found also that $C_3 = C_5 = 0$. Thus, the displacement field in the central isotropic cylinder is

$$u = C_1 r, \quad v = \vartheta r z, \quad w = Cz. \tag{40}$$

as expected.

For the anisotropic shell, only the displacement $U(r)$ is uncoupled. The components of $V(r)$ and $W(r)$ are computed using Eq. (37). Substituting Eq. (37) into Eq. (2), we obtain the characteristic equation.

$$(c_{66}\alpha^2 - c_{66})\overline{V} + (c_{56}\alpha^2 + c_{56}\alpha)\overline{W} = 0, \tag{41}$$

$$(c_{56}\alpha^2 - c_{56}\alpha)\overline{V} + c_{55}\alpha^2\overline{W} = 0. \tag{42}$$

Solving for α, we find the roots $\alpha = 0,0,1,-1$. The solution to $V(r)$ and $W(r)$ becomes

$$V(r) = V_1 + V_2 \ln r + V_3 r + \frac{V_4}{r}, \tag{43}$$

$$W(r) = W_1 + W_2 \ln r + W_3 r + \frac{W_4}{r}, \tag{44}$$

where V_1, V_2, V_3, V_4, W_1, W_2, W_3 and W_4 are constant so far undefined.

With no rigid body movement, $V_1 = W_1 = 0$. To match the stresses τ_{rz} and $\tau_{r\theta}$ of the isotropic part at $r = r_1$, which are equal to zero, constants V_4 and W_2 must be zero as well. Since V_2 and W_4 are linearly dependent to W_2 and V_4, they also must be zero. Hence, the displacements of the anisotropic part is

$$U(r,\theta) = C_1 r^k + C_2^{-k} - c_{11} m_1 r^2 - 4c_{11} m_2 r + m_1 c_{22} r^2 + m_2 c_{22} r,$$
$$V(r,\theta) = \vartheta r z, \quad W(r,\theta) = zC,$$

where

$$k = \sqrt{\frac{c_{22}}{c_{11}}}, \quad m_1 = \frac{2\vartheta(c_{14} - \frac{1}{2}c_{24})}{(c_{22} - c_{11})(c_{22} - 4c_{11})}, \tag{45}$$

$$m_2 = \frac{C(c_{13} - c_{23})}{(c_{22} - c_{11})(c_{22} - 4c_{11})}. \tag{46}$$

The remaining unknown constants are found using the boundary conditions in Eqs. (5) and (7).

3.2. Displacements under pure bending

Under the bending moment M, the assumed solution is:

$$U(r,\theta) = \overline{U} r^\alpha \sin\theta, \quad V(r,\theta) = \overline{V} r^\alpha \cos\theta, \quad W(r,\theta) = \overline{W} r^\alpha \cos\theta.$$

Substituting Eq. (47) into the equilibrium equation Eq. (2), we obtain the characteristic system

$$(c_{11}\alpha^2 - c_{66} - c_{22})\overline{U} - (c_{12}\alpha + c_{66}\alpha - c_{66} - c_{22})\overline{V} - (c_{14}\alpha + c_{56}\alpha - c_{24})\overline{W} = 0,$$
$$(c_{66}\alpha + c_{66} + c_{12}\alpha + c_{22})\overline{U} + (c_{66}\alpha^2 - c_{66} - c_{22})\overline{V} + (c_{56}\alpha^2 + c_{56}\alpha - c_{24})\overline{W} = 0,$$
$$(c_{56}\alpha + c_{14}\alpha + c_{24})\overline{U} + (c_{56}\alpha^2 - c_{56}\alpha - c_{24})\overline{V}(c_{55}\alpha^2 - c_{44})\overline{W} = 0,$$

where c_{ij} are the components from the stiffness matrix **C** in Eq. (16).

The quantities c_{14}, c_{24}, c_{34} and c_{56} are zero in the case of the isotropic material. For anisotropic shell, the system of equations can be rewritten in the matrix form:

$$\begin{bmatrix} H_{11}(\alpha) & H_{12}(\alpha) & H_{13}(\alpha) \\ H_{21}(\alpha) & H_{22}(\alpha) & H_{23}(\alpha) \\ H_{31}(\alpha) & H_{32}(\alpha) & H_{33}(\alpha) \end{bmatrix} \begin{bmatrix} \overline{U} \\ \overline{V} \\ \overline{W} \end{bmatrix} = \begin{bmatrix} 0 \\ 0 \\ 0 \end{bmatrix}. \tag{47}$$

where H_{ij} are the coefficients of $\overline{U}$, $\overline{V}$, and $\overline{W}$ shown in Eq. (47). Setting det **H** = 0 and solving for α, we find that α has six roots: a double root at zero and two mutually opposite real pairs $\pm\alpha_1$ and $\pm\alpha_2$. The exponent α in Eq. (50) are expressed as

$$\alpha = 0, 0, \pm 2a_1\sqrt{-a_2 + \sqrt{a_2^2 - 4a_1 a_3}}, \pm 2a_1\sqrt{a_2 - \sqrt{a_2^2 - 4a_1 a_3}}, \tag{48}$$

where

$$
\begin{aligned}
a_1 &= c_{11}\left(c_{55}c_{66} - c_{56}^2\right),\\
a_2 &= c_{11}\left(c_{56}^2 - c_{44}c_{66} + 2c_{56}c_{24}\right) - \left(c_{11}c_{55} + c_{55}c_{66} - c_{56}^2\right)b_1 +\\
&\quad + b_2^2 c_{55} + b_3^2 c_{66} - 2b_2 b_3 c_{56},\\
a_3 &= b_1\left(c_{11}c_{44} + c_{44}c_{66} - c_{56}^2 - b_3^2 + 2b_3 c_{56}\right) -\\
&\quad - b_2(b_2 c_{44} - 2b_3 c_{24} + 2c_{24}c_{56}) - c_{24}^2(c_{11} - c_{66}),\\
b_1 &= c_{22} + c_{66}, \quad b_2 = c_{12} + c_{66}, \quad b_3 = c_{14} + c_{56}.
\end{aligned}
$$

Finally, the displacements are expressed as

Isotropic solid cylinder:

$$
\begin{aligned}
&U(r,\theta) = \left(U_I r^{\alpha} - \frac{B\nu r^2}{2}\right)\sin\theta, \quad V(r,\theta) = \left(V_I r^{\alpha} + \frac{B\nu r^2}{2}\right)\cos\theta,\\
&W(r,\theta) = W_I r\cos\theta,
\end{aligned} \tag{49}
$$

Anisotropic helicoidal layer:

$$
\begin{aligned}
U(r,\theta) &= \left(U_1 r^{\alpha_1} + U_2 r^{-\alpha_1} + U_3 r^{\alpha_2} + U_4 r^{-\alpha_2} + U_p r^2\right)\sin\theta,\\
V(r,\theta) &= \left(V_1 r^{\alpha_1} + V_2 r^{-\alpha_1} + V_3 r^{\alpha_2} + V_4 r^{-\alpha_2} + V_p r^2\right)\cos\theta,\\
W(r,\theta) &= (W_1 r^{\alpha_1} + W_2 r^{-\alpha_1} + W_3 r^{\alpha_2} + W_4 r^{-\alpha_2} + W_p r^2)\cos\theta,
\end{aligned} \tag{50}
$$

The unknown constants, U_i, V_i, and W_i (i = 1..4), which are linearly dependent to each other, are determined from the boundary conditions Eqs. (5) and (7). The constants U_p, V_p, W_p are found from the loading conditions Eq. (9).

Having obtained the displacements $U(r,\theta)$, $V(r,\theta)$, and $W(r,\theta)$, stresses could be found by substituting Eq. (3) into Eq. (4).

4. Numerical simulations: stress fields computation and finite element method

Consider a cylinder made of aluminum 6061-T6 enveloped by a T300/862 graphite/epoxy shell having a fiber oriented an angle ϕ. The data used in the current numerical example are shown in Tables 1–3 [8].

The comparison of stresses between the elasticity and finite element analysis are shown in Figs. 5 and 6. The results are taken at a distance $z = l_o$ from the fixed end so that the Saint–Venant's principle is valid. The value $l_0 = 0.1$ L is used in this analysis since it is the closest location to the fixed end where the surface of the structure is free of stresses σ_{rr} and $\sigma_{r\theta}$. Figs. 5, 6 show that the analytical solution and finite element solution converge to each other both for axial loading and for the pure bending case. For axial loading case, σ_{zz} has the highest value when spiral angle is zero and decreases as the spiral angle increases. When the spiral angle is 90°, the tangential stress shows the highest value. Similar behavior can also be found in the bending case. For both cases, the stress $\sigma_{\theta\theta}$ changes sign at 60°, while the stress $\sigma_{\theta z}$ changes sign at approximately 63°. Between the spiral angle of 20–50°, the order of magnitude of stresses in the axial loading case is relatively close to one another. On the other hand, the same is not observed for the bending case. It should be noted that these results are valid only for the case of small deformations.

5. Equivalent link model

It is convenient to replace the three-dimensional cylinder with a link. The helicoidal symmetry results in a coupling between a rotation about the axis and the elongation as shown in Fig. 7. Linkages are useful for describing the physics of a larger structure that is assembled from multiple links where the displacement and reactions at their ends are of major interests.

Table 1
Parameters for the geometry and the applied load

Parameter	Value	
	U.S. customary units	SI units
Outer radius of the cylinder (r_1)	0.25 in.	6.35 mm
Inner radius of the shell (r_2)	0.25 in.	6.35 mm
Outer radius of the shell (r_3)	0.3125 in.	7.94 mm
Length (L)	5 in.	127 mm
Axial load (P)	1000 lb.	4448 N
Bending moment (M)	500 lb.in.	56.5 N · m

Table 2
Aluminum 6061-T6 properties

Parameter	Value	
	US customary units	SI units
E	10 Msi	68.95 GPa
G	3.7 Msi	25.5115 Gpa
v	0.35	0.35

Table 3
T300/862 material properties

Parameter	Value	
	US customary units	SI units
$E_{11} = E_{22}$	1.101 Msi	7.591 GPa
E_{33}	20.21 Msi	139.348 GPa
$G_{23} = G_{13}$	0.5495 Msi	3.789 GPa
G_{12}	0.4035 Msi	2.782 GPa
$v_{23} = v_{13}$	0.0178	0.0178
v_{12}	0.3642	0.3642

We obtain the stiffness matrix $\mathbf{k}$ that links the force P and the moment M at the element ends to the elongation u and the rotation about the axis θ,

$$\mathbf{f} = \mathbf{k}\mathbf{u} \text{ or } \begin{Bmatrix} P \\ M \end{Bmatrix} = \begin{bmatrix} k_1 & k_2 \\ k_4 & k_3 \end{bmatrix} \begin{Bmatrix} u \\ \theta \end{Bmatrix}. \tag{51}$$

The quantities of interest are the stiffness constants, k_1, k_2, k_3 and k_4. However, it can be shown that the stiffness matrix is symmetric using the minimum potential energy principle. The total potential energy of the structure shown in Fig. 7 is expressed as

$$\pi_p = \frac{1}{2}\mathbf{u}^{\mathrm{T}}\mathbf{k}\mathbf{u} - \mathbf{f}\mathbf{u} = \frac{1}{2}[u \quad \theta] \begin{bmatrix} k_1 & k_2 \\ k_4 & k_3 \end{bmatrix} \begin{Bmatrix} u \\ \theta \end{Bmatrix} - [P \quad M] \begin{Bmatrix} u \\ \theta \end{Bmatrix} = \frac{1}{2}\left(k_1 u^2 + (k_2 + k_4)u\theta + k_3\theta^2\right) - Pu - M\theta. \tag{52}$$

Without losing the generality, one can assume that $k_4 = k_2$, and the stiffness matrix $\mathbf{k}$ can be rewritten as

$$\mathbf{k} = \begin{bmatrix} k_1 & k_2 \\ k_2 & k_3 \end{bmatrix}. \tag{53}$$

These stiffness values can also be found analytically, using the formulas obtained in Sections 3.1 and 3.2. However, we show another way to obtain them here. By taking two measures of P (P_1 and P_2) and M (M_1 and M_2), and rearranging Eq. (51), the system $\mathbf{f} = \mathbf{u}\mathbf{k}$ that has four equations and three unknowns (k_1, k_2, and k_3) is obtained:

$$\begin{Bmatrix} P_1 \\ M_1 \\ P_2 \\ M_2 \end{Bmatrix} = \begin{bmatrix} u_1 & \theta_1 & 0 \\ 0 & u_1 & \theta_1 \\ u_2 & \theta_2 & 0 \\ 0 & u_2 & \theta_2 \end{bmatrix} \begin{Bmatrix} k_1 \\ k_2 \\ k_3 \end{Bmatrix}, \tag{54}$$

where u_1, u_2, θ_1 and θ_2 are the displacements corresponding to the loads P_1, P_2, M_1 and M_2, and are computed from the elasticity solution discussed in the earlier sections. The expression Eq. (54) is overdetermined because it gives four equations in three unknowns, and thus may have no solution. However, we can multiply the system by $\mathbf{u}^{\mathbf{T}}$ and solve for the unknown $\mathbf{k}$, which leads to the expression of the least square solution,

$$\begin{aligned} &\mathbf{u}^{\mathrm{T}}\mathbf{f} = \mathbf{u}^{\mathrm{T}}\mathbf{u}\mathbf{k} \\ &(\mathbf{u}^{\mathrm{T}}\mathbf{u})^{-1}\mathbf{u}^{\mathrm{T}}\mathbf{f} = (\mathbf{u}^{\mathrm{T}}\mathbf{u})^{-1}\mathbf{u}^{\mathrm{T}}\mathbf{u}\mathbf{k} \\ &\mathbf{k} = (\mathbf{u}^{\mathrm{T}}\mathbf{u})^{-1}\mathbf{u}^{\mathrm{T}}\mathbf{f}. \end{aligned} \tag{55}$$

Eq. (55) minimizes the error $\mathbf{e} = \mathbf{f} - \mathbf{u}\mathbf{k}$ that is produced by the solution to this overdetermined system.

Taking the displacements u and θ that correspond to the loads P and M from the closed-form analytical solution (obtained in Section 3.1) and substituting them into Eq. (55), the stiffness k_1, k_2, and k_3 can be determined. The one-dimensional equivalent results based on the geometries and the materials discussed in previous section are shown below as an example (Fig. 8). These plots demonstrate how the stiffness values vary with the spiral angle. The values of the stiffness also vary linearly with

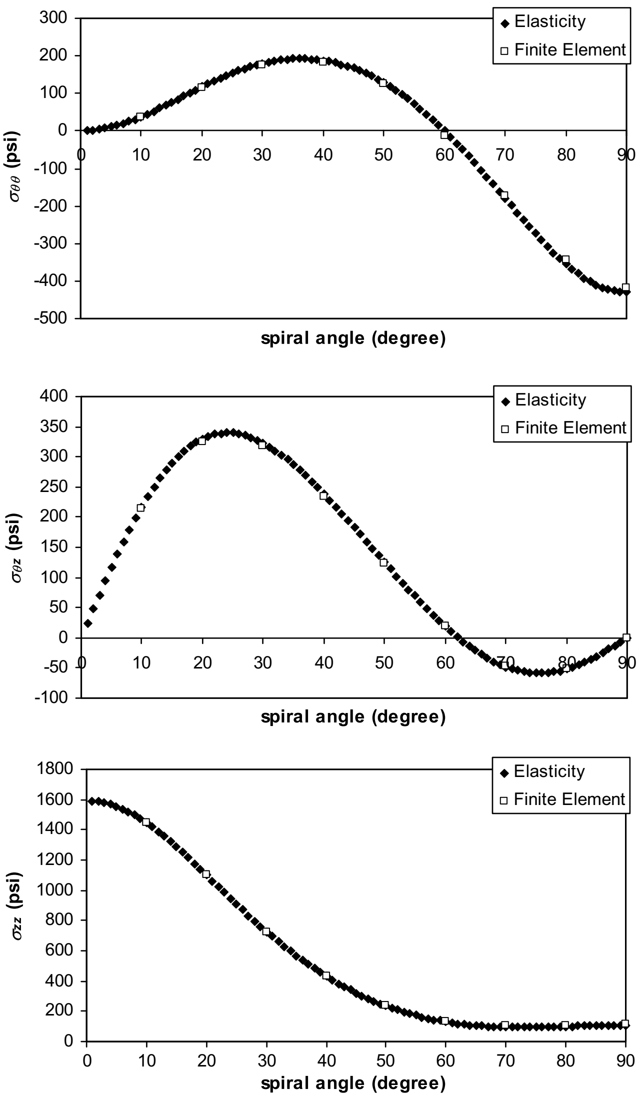

Fig. 5. Comparison of stresses under axial loading.

the load P and the length L of the three-dimensional model. Despite having only an axial load applied, the stiffness k_2 and k_3 generate rotation as the structure is stretched.

We realize that the effect of coupling increases the energy release capability while the elongation can remain the same. The additional twisting degrees of freedom correspond to additional energy released in the process of elongation.

6. Application of a link model: 1-D finite element formulation

Consider a one-dimensional structural element shown in Fig. 9 where axial deformation is coupled with the rotation about the generator. The deformations are represented by

$$\delta = \hat{d}_{2x} - \hat{d}_{1x} \quad \text{and} \quad \gamma = \hat{\phi}_{2x} - \hat{\phi}_{1x}, \tag{56}$$

where δ and γ are elongation and rotation, respectively. The local axial displacement is represented by $\hat{d}$ while the nodal rotation is represented by $\hat{\phi}$. The force-displacement relationship is expressed as

$$P = k_1\delta + k_2\gamma, \quad \text{and} \quad M = k_2\delta + k_3\gamma, \tag{57}$$

where P and M are axial and torsional loads, respectively. The quantities k_1, k_2, and k_3 are the stiffness constants. Substituting Eq. (56) into Eq. (57), we have

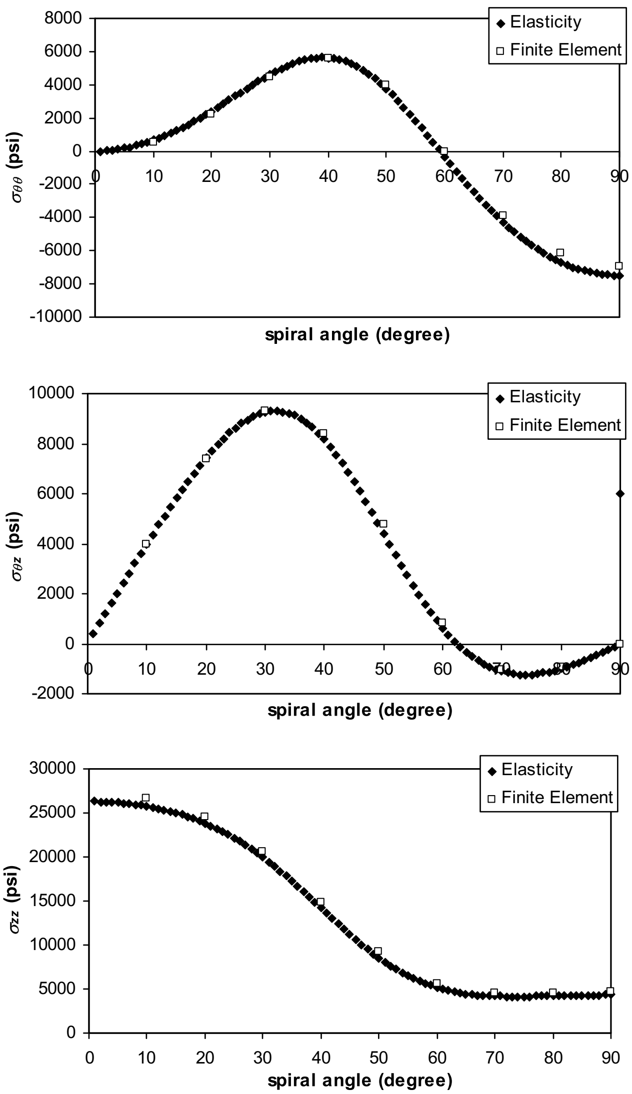

Fig. 6. Comparison of stresses under pure bending.

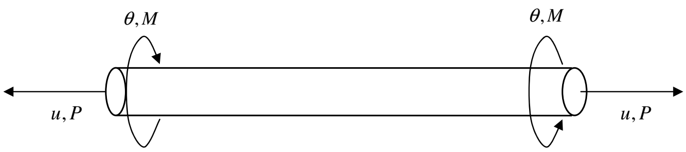

Fig. 7. One-dimensional structural model.

$$P = k_1(\hat{d}_{2x} - \hat{d}_{1x}) + k_2(\hat{\phi}_{2x} - \hat{\phi}_{1x}), \tag{58}$$
$$M = k_2(\hat{d}_{2x} - \hat{d}_{1x}) + k_3(\hat{\phi}_{2x} - \hat{\phi}_{1x}). \tag{59}$$

By the sign convention for the nodal forces and equilibrium,

$$\hat{f}_{1x} = -P, \quad \hat{f}_{2x} = P, \quad \hat{m}_{1x} = M, \quad \hat{m}_{2x} = -M. \tag{60}$$

Rewriting Eq. (59) and expressing it in the matrix form

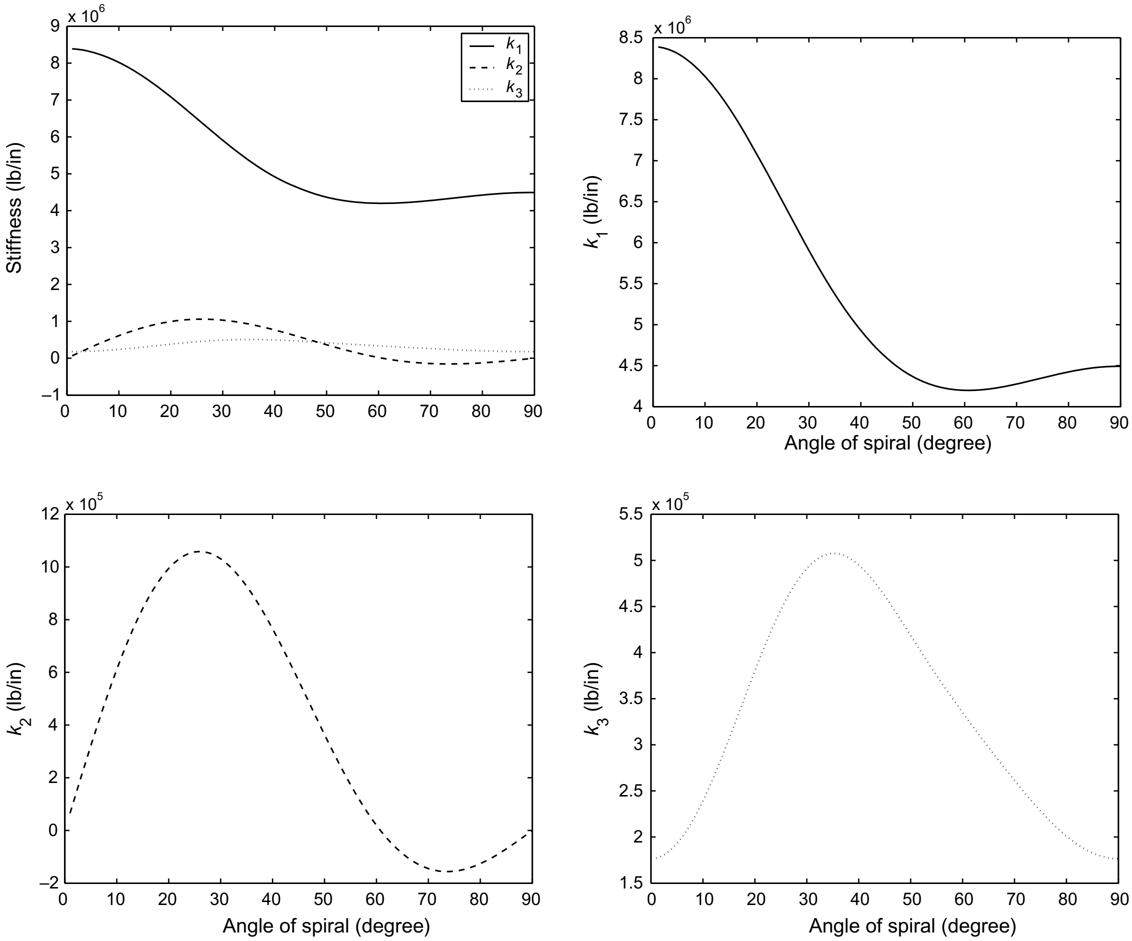

Fig. 8. Stiffnesses of the one-dimensional model.

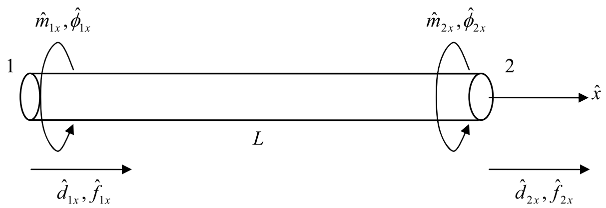

Fig. 9. One-dimensional structural element.

$$\begin{Bmatrix} \hat{f}_{1x} \\ \hat{m}_{1x} \\ \hat{f}_{2x} \\ \hat{m}_{2x} \end{Bmatrix} = \begin{bmatrix} k_1 & k_2 & -k_1 & -k_2 \\ k_2 & k_3 & -k_2 & -k_3 \\ -k_1 & -k_2 & k_1 & k_2 \\ -k_2 & -k_3 & k_2 & k_3 \end{bmatrix} \begin{Bmatrix} \hat{d}_{1x} \\ \hat{\phi}_{1x} \\ \hat{d}_{2x} \\ \hat{\phi}_{2x} \end{Bmatrix}. \tag{61}$$

Hence, the element stiffness matrix is defined as

$$\hat{\mathbf{k}} = \begin{bmatrix} k_1 & k_2 & -k_1 & -k_2 \\ k_2 & k_3 & -k_2 & -k_3 \\ -k_1 & -k_2 & k_1 & k_2 \\ -k_2 & -k_3 & k_2 & k_3 \end{bmatrix}, \tag{62}$$

where k_1, k_2 and k_3 are the values calculated from the one-dimension structural model. The nodal displacements are then determined by solving the system $\hat{\mathbf{f}} = \hat{\mathbf{k}}\hat{\mathbf{u}}$.

7. Significance of spiralling grain in a tree's trunk

We observe spirals in many structures in nature. Some examples are grains of pine trees that wind around its body, the horn-like tooth of narwhal whale, or a sea sponge skeleton, (Fig. 2). One wonders what the evolutionary significance of such design is. We expect that there must be a good evolutionary reason for a natural design to becomes more complex.

Studying morphology of bones or trees'trunks that are critical for the survival of the species, we may postulate that they are optimally adapted to the environment and treat the evolutionary development as a minimizing sequence of an optimization problem with unknown objective [9]. The optimization problems in engineering and in biology are mutually reciprocal. The biological structure is known, but it is not clear in what sense the structure is optimal. By contrast, the goal of the engineering is the minimization of a given functional that is not the subject of a search; the problem is to find an unknown optimal structure.

Trees' trunks should stay unbroken and be able to sustain extreme wind loads from all directions. Their grains should be able to efficiently transport water to feed branches. We notice that some trees have grains spiralling around their trunk, such as Ponderosa pine that grows in rocky and windy terrains in Southwestern of the United States (Utah, Arizona, Nevada). These observations lead to questions: Why does the grain in trees spiral? and What is "the best" spiralling angle?

It was observed by Kubler [10] that spiralling leads to better distribution of water for the case where the tree roots on one side are not functional. The efficiency of the water transportation is proportional to the length of the grain. The biological factor of the spiral formation of the grains was investigated by Schulgasser [11].

In our previous paper [2], we demonstrated that the strength of the trunk depends on spiralling grain angle. Now, we examine the deformations of the trunk and argue that the spiralling is beneficial since it allows for larger deformations that release excessive energy and help removing extra weight such as snow from the branches.

Here, we examine whether the design of the trunk corresponds to a solution of the following structural optimization problem:

> Given an axisymmetric cylinder (the trunk) from an orthotropic elastic material (the wood), find an angle of spiralling (inclination of the main axes of orthotropy to the cylinder's axes), which increases flexibility and does not significantly increase the length of the grains.

The displacement fields of the tree trunk is determined using nonlinear finite element method (FEM) that is verified by analytical solution presented in [7]. Rather than finding the solutions of the axial and bending load case separately, the problem for the combined loads is solved. The Tsai-Hill failure criterion is used to predict the failure as a function of the grain angle based on the gross mechanical strength using the mechanics of materials approach.

8. Analysis

The analysis of the mechanical model uses the following assumptions:

- The Ponderosa pine trunk is modelled as a cylinder shown in Fig. 3.
- The torsional load is neglected: Branches are symmetric around the circumference.
- The grain angle does not change radially or axially.
- There are no body forces: all the weight comes from the crown.

We also make a technical assumption. To avoid the singularity at the center of the circular cross-section of the trunk, we assume that the isotropic material with the same modulus as the grain of tree is placed in a small central circle (its diameter is 5% of the diameter of the trunk).

8.1. Nonlinear stress analysis

The linear analysis of stresses in helicoidally orthotropic elastic cylinder is found in [2]. It is applicable when the deformation is small. However, when the transverse deflection is large, a significant extra moment is generated by the axial load and the problem becomes nonlinear. Here, we perform the nonlinear analysis using finite element method (FEM). A 3-D eight node element shown in Fig. 10 is used for the computation. This element has three degrees of freedom, u, v, and w:

$$\begin{Bmatrix} u \\ v \\ w \end{Bmatrix} = \sum_{i=1}^{8} \begin{bmatrix} N_i & 0 & 0 \\ 0 & N_i & 0 \\ 0 & 0 & N_i \end{bmatrix} \begin{Bmatrix} u_i \\ v_i \\ w_i \end{Bmatrix} + \sum_{j=9}^{11} \begin{bmatrix} N_j & 0 & 0 \\ 0 & N_j & 0 \\ 0 & 0 & N_j \end{bmatrix} \begin{Bmatrix} u_j \\ v_j \\ w_j \end{Bmatrix}. \tag{63}$$

The shape functions are

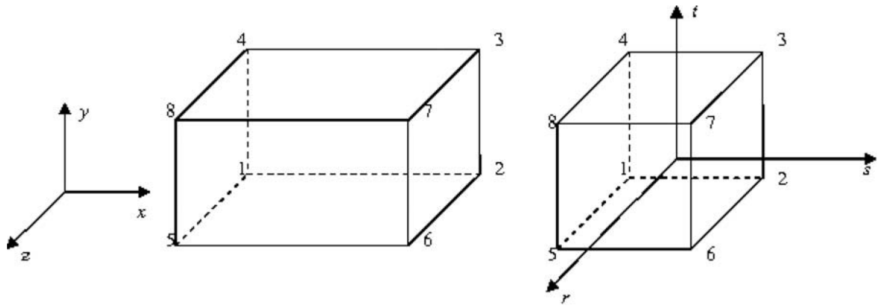

Fig. 10. Sketch of element in global-coordinate system (x, y, z) and local-coordinate element (r, s, t).

$$\begin{aligned}
N_1 &= \frac{1}{8}(1-s)(1-t)(1-r), \quad N_2 = \frac{1}{8}(1+s)(1-t)(1-r) \\
N_3 &= \frac{1}{8}(1+s)(1+t)(1-r), \quad N_4 = \frac{1}{8}(1-s)(1+t)(1-r) \\
N_5 &= \frac{1}{8}[(1-s)(1-t)(1+r) + (1-s)(1-t)(1+r)] \\
N_6 &= \frac{1}{8}[(1+s)(1-t)(1+r) + (1+s)(1-t)(1+r)] \\
N_7 &= \frac{1}{8}(1+s)(1+t)(1+r), \quad N_8 = \frac{1}{8}(1-s)(1+t)(1+r) \\
N_9 &= \frac{1}{8}(1-s^2), \quad N_{10} = \frac{1}{8}(1-t^2), \quad N_{11} = \frac{1}{8}(1-r^2),
\end{aligned} \tag{64}$$

where the parameter (r, s, t) are local-coordinates of the element. Unlike the conventional shape functions of an eight-node element, we use eleven shape functions for the element. The shape functions with indices 9–11 represent the extra terms that lessen the stiffness of the conventional linear hexahedral element.

The boundary conditions for the calculation are shown in Fig. 11. At $z = 0$, the displacements are $u = v = w = 0$, and the loads are applied at the free end $z = L$. The load P is a result from a surface pressure q, while the moment M is generated by an applied couple f.

8.2. Failure criteria

Due to anisotropy of wood, the conventional maximum strength criterion for isotropic materials gives a poor prediction of failure. Instead, Tsai-Hill failure criterion is used

$$\left(\frac{\sigma_1}{\sigma_{1u}}\right)^2 + \left(\frac{\sigma_2}{\sigma_{2u}}\right)^2 - \frac{\sigma_1\sigma_2}{\sigma_{1u}^2} + \left(\frac{\tau_{12}}{\tau_{12u}}\right)^2 < 1 \tag{65}$$

Here, subscripts 1, 2, and 12 indicates the fiber (grain), transverse, and shear direction. Stresses in the denominator of Eq. (65) are equal to the ultimate strength of the material in these directions. When the left-hand side of Eq. (65) is greater than or equal to one, the failure is predicted. No distinction is made between compressive and tensile stresses. Here we only investigate the failure based on the gross strength of the tree. Our goal is to relate the angle of the spiralling grains to overall strength of the tree.

9. Numerical analysis of Ponderosa pine

Ponderosa pines average 100–160 ft (30.47–48.77 m) in height, and 2–4 ft (0.61–1.22 m) in diameter [12]. This analysis categorizes the Ponderosa pine into three size classes according to [13], (see also Table 4).

The magnitude of axial load P is measured from the average weight of the crown that the Ponderosa pines of this size may experience [13]. Typical maximum wind speed in Southern Utah is measured at 35 m/s (78.75 mph) [14]. The air density ρ and viscosity μ are assumed to be 1.23 kg/m^3 and 1.78×10^{-5} kg/m · s. For instance, assuming a uniform air flow, the Reynolds number, Re, for the diameter of 0.9398 m is approximated as

$$Re = \frac{2\rho v r}{\mu} = 2.273 \times 10^6 \geqslant 10^4,$$

The drag coefficient C_D of a cylinder is 1.2 for $Re \geqslant 10^4$. Thus,

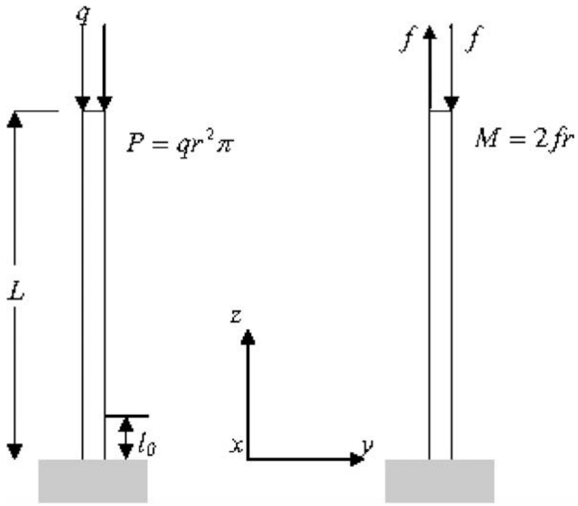

Fig. 11. Free body diagrams the numerical model.

Table 4
Code number for size class

Size class	Diameter at breast height (m)
2	0.1270–0.2794 (5–11 in.)
3	0.3048–0.5080 (12–20 in.)
4	<0.5080 (20 in.)

Table 5
Applied loads and Ponderosa pine sizes

Size class	Diameter (m)	Height (m)	Crown weight (N)	Bending moment (N m)
2	0.2286	10.67	556.8	11760
3	0.4826	16.76	3065	61310
4	0.9398	35.36	13410	531100

Table 6
Ponderosa pine material strengths (MPa)

σ_{33t}	σ_{33c}	σ_{22t}	σ_{22c}	τ_{23_u}
43	−36	2.8	−5.1	8

$$F_D = \frac{1}{2} C_D A \rho v^2 = \frac{1}{2}(1.2)(0.9398)(35.36)(1.23)(35)^2$$
$$= 30040\ \text{N}$$
$$M = \frac{F_D h}{2} = (30040)(35.36/2) = 531100\text{N} \cdot \text{m},$$

where A is the frontal area, F_D is the drag force, and M is the bending moment. Table 5 shows the loads used in the analysis for each size class:

Table 7
Modulus of elasticity of Ponderosa pine with 12% moisture content (GPA)

E_1	E_2	E_3	G_{12}	G_{13}	G_{23}
0.85	0.51	10.1	0.065	0.71	0.67

Table 8
Poisson's ratio of Ponderosa pine with 12% moisture content

ν_{31}	ν_{32}	ν_{12}	ν_{21}	ν_{13}	ν_{23}
0.337	0.4	0.426	0.359	0.41	0.033

This approximation shows the order of magnitude of the bending moment that the Ponderosa pine in Southern Utah may experience. The material properties of the Ponderosa pine are computed from the data given in [15,16] and are shown in Tables 6–8.

10. Results and discussion

First, we mention the effect of the extra shape functions in Eq. (64). Fig. 12 shows the comparison of the finite element model with and without the extra shape functions when the spiralling angle is 50°. Without the extra shape functions, the model significantly under-estimates the transverse displacement. The required number of nodes and elements has to be in-

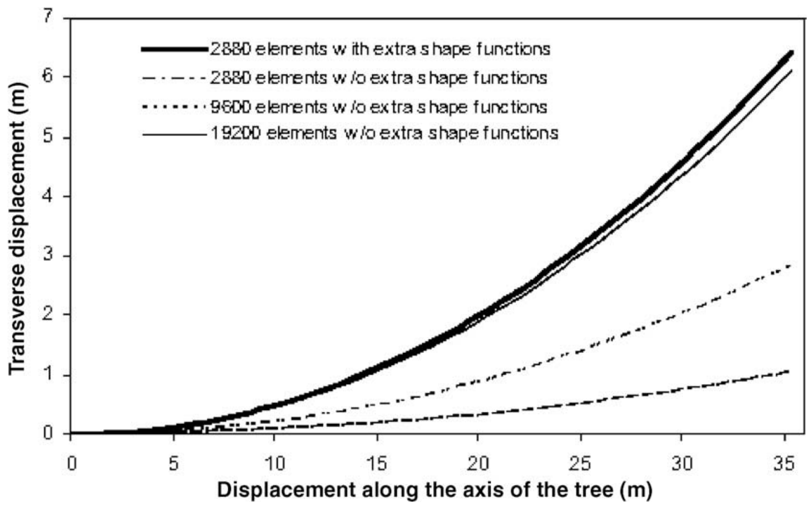

Fig. 12. Transverse displacement along the axis of the tree when spiralling angle is 50°.

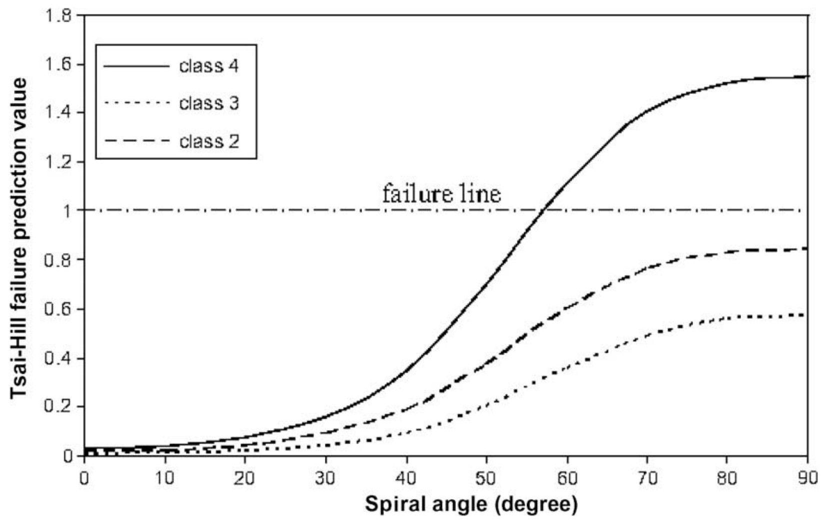

Fig. 13. Failure prediction value for spiralling angle from 0° to 90°.

creased by about seven times in order to obtain converged results. Utilizing the extra shape functions, the number of elements and node are kept low and the computational time is reduced significantly.

The results of the spiralling angle of the grains are analyzed based on the following criteria:

(i) Composite failure – gives the bound for the maximum angle.
(ii) Transverse deflection – shows flexibility of the tree.
(iii) Minimum grain length – gives the efficient of the water transportation to crown.

Finally, the combined criterion is constructed to show the optimize angle of spiralling.

10.1. Failure criterion

Fig. 13 illustrates that the Tsai-Hill value increases slowly to about 30°, and then increases dramatically beyond this point. For the given wind load, only class 4 Ponderosa pine shows value that exceeds unity. The limiting spiralling angle cannot be seen from results of the smaller classes. The class 4 Ponderosa pine has limiting spiralling angle of 55°.

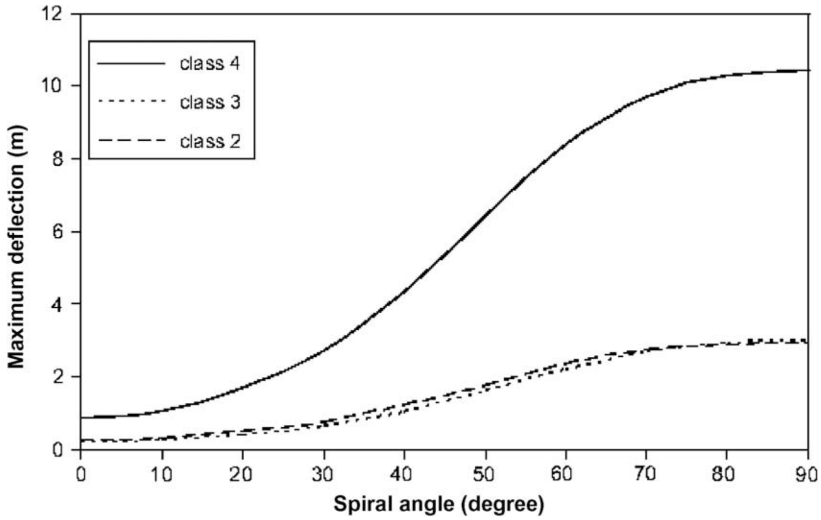

Fig. 14. Maximum transverse deflection.

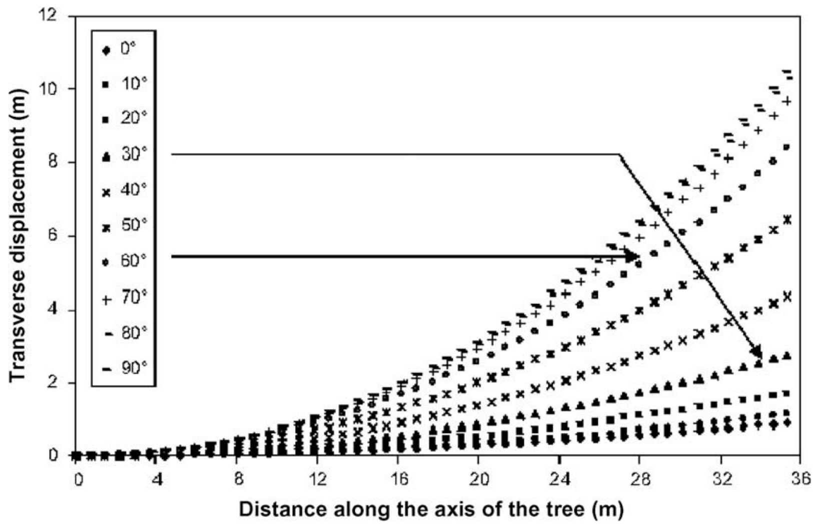

Fig. 15. Transverse displacement along the axis of the tree (class 4 sample).

10.2. Transverse displacement and the tree's flexibility

To study the effect that spirals have on the structural flexibility of the tree, the transverse displacement is computed using nonlinear FEM where the combined loadings of axial load and bending moment are applied. The maximum displacements at various angle are shown in Fig. 14. Notice that the maximum deflections of class 2 and 3 are very small when compared to class 4. The data given in Table 5 shows that the height and the trunk's diameter are not proportional to each other.

In addition, detailed plots of displacement v of class 4 (largest size) Ponderosa pine is presented in Fig. 15. Spiralling is needed to generate enough deflection so that the tree does not risk failure, allowing trees in nature to be able to carry excessive weights (such as snow) and withstand high winds. Fig. 15 shows a large increase in the magnitude of the transverse deflection when the grain angles increase from 30° to 60° in comparison to the smaller change at other intervals of the spiralling angle.

10.3. Water transportation criterion and effectiveness of the spiralling grains

One of the vital purposes of the grains is to transport water from the roots to branches. The effectiveness of the fluid transportation is proportional to the length of the path. This length increases with the angle. For a given height of a tree, the length is

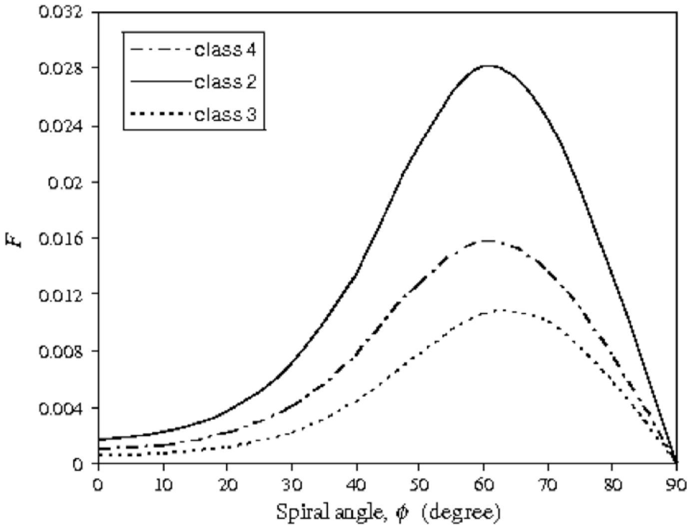

Fig. 16. Ratio of failure prediction value to length of grain versus spiralling angle.

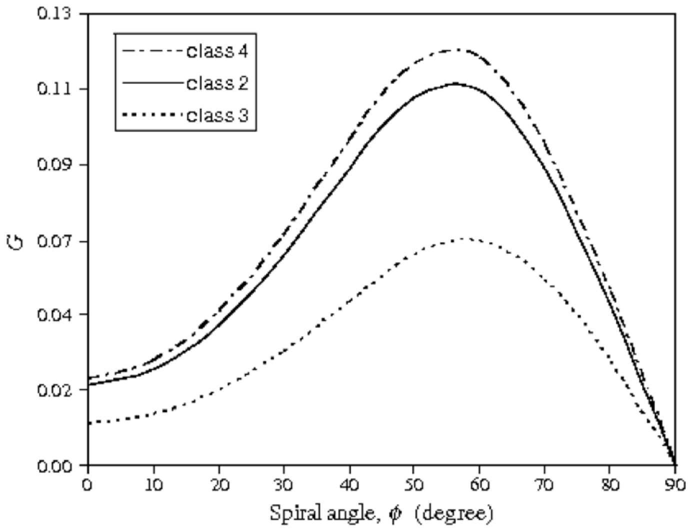

Fig. 17. Ratio of maximum deflection to length of grain versus spiralling angle.

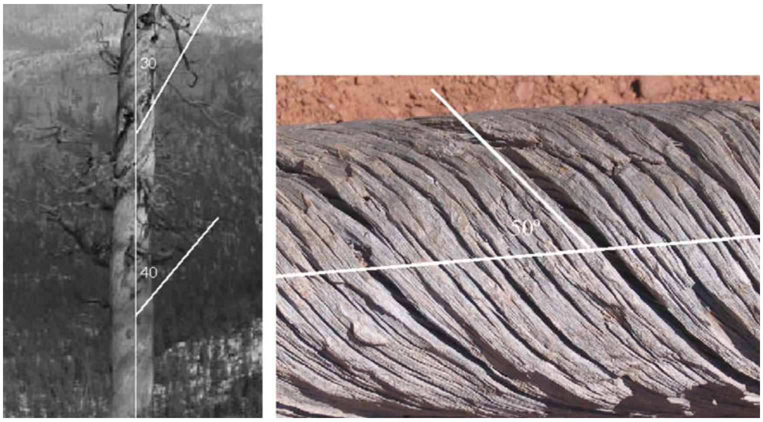

Fig. 18. Measurement of angle of spiral.

$$L = 2\frac{\pi r}{\sin\phi}. \tag{66}$$

10.4. Combined criteria

Let us compare the "effectiveness" of various helicoidal trunks. The ideal design combines the high value of predicted failure value and the small length of the path along the grain that provides efficient water transportation. Combining these criteria, we choose the functional $F(\phi)$ equal to the ratio of the Tsai-Hill failure prediction value and the path length of a grain

$$F = \frac{\text{predicted failure value}}{L}. \tag{67}$$

A similar criterion is set for deflection the path length of a grain. The ideal design combines the large deflection and small length of the path along the grain. The corresponding criterion takes the form

$$G = \frac{\text{deflection}}{L}. \tag{68}$$

The graphs are shown in Figs. 16 and 17. This criterion suggests that the most "effective" spiralling angle of the grain is in the range of approximately 50–60° for class 4 pine.

11. Conclusion

- A linear elastic helicoidal orthotropic cylinder is considered and closed-form analytical expression for the displacement is found. The analytic solution is valid. It is suitable for investigation of the influence of the spiralling and optimization of that angle. It reveals the dependence of elastic constant of the spiralling angle.
- The results are verified by comparing the finite elements solution with the analytical solution. The analytical solution requires less computational time but the finite element solution can handle the nonlinear model.
- A link model is developed that connects the displacement and rotation of the cylinder's end with the applied force and moment. This model can be used as a component of a larger structure or in finite element formulation.

Our analysis shows that the limiting angle is 55° for a full grown Ponderosa pine. Based on Fig. 16, spiralling angle decreases as the size of the tree increases. Spiralling angles smaller than 30° are not beneficial according to the two combined criteria F and G presented here. Most Ponderosa pines observed in Southern Utah show the spiralling of the grain at angle between 30° and 50°. Fig. 18 shows example of Ponderosa pine having grain spiralling between 30° and 40°.

Here we investigate a Ponderosa pine from a mechanical perspective, and no other factors are accounted for. The list of other factors that are not considered in this analysis are as follow:

- In nature, the grain angle is larger toward the bottom of the tree and reduces with position up the length of the trunk. We speculate that when the tree is small, it requires more distribution of fluid to ensure proper growth. Hence, having the grain spiralling at a larger angle allows the tree to transport more fluid along its circumference. As the tree grows taller, the angle becomes smaller, which reduces the coverage area allowing the fluid to be transported to the higher portion faster.

– The cracking of the tree trunk, which may be an important factor, is not considered in this analysis. Looking at the elastic constants of the Ponderosa pine, one finds that the transverse modulus E_2 is approximately 5% of the grain modulus E_3. This ratio can be viewed as if there were a crack. As the crack propagates around the tree, it is less prone to fracture than when the grain and the crack are vertical.

This analysis shows that the question of the adaptation of a tree trunk can be considered as a problem of constrained minimization. The combined criteria provide a range of beneficial angles of the spirals. A structure can become more flexible by having the grains spiral along its circumference. The grain length limits the angle range from above.

References

[1] X. Chen, S. Zhang, D.A. Dikin, W. Ding, R.S. Ruoff, Mechanics of a carbon nanocoil, Nano Letters 3 (2003) 1299–1304.
[2] S. Leelavanichkul, A.V. Cherkaev, Why the grain in tree trunk spirals: a mechanical perspective, Structural and Multidisciplinary Optimization 28 (2004) 127–135.
[3] S.G. Lekhnitskii, Theory of Elasticity of an Anisotropic Elastic Body, Gostekhizdat, Moscow, 1963. (in Russian).
[4] S.G. Lekhnitskii, Theory of Elasticity of an Anisotropic Body, MIR Publishers, Moscow, 1981.
[5] S.G. Lekhnitskii, Anisotropic Plate, Gostekhizdat, Moscow, 1957. (in Russian).
[6] N.J. Pagano, The stress field in a cylindrically anisotropic body under two dimensional surface tractions, Journal of Applied Mechanics (1972) 791–796.
[7] S. Leelavanichkulss. Helicoidal Morphology in Engineering Structure, Dissertation, University of Utah, 2007.
[8] J.M. Starbuck, C. Eberle, Analytical solution for the design of spoolable composite tubing, Mechanics of Materials 3.
[9] A.V. Cherkaev, L.I. Slepyan, Waiting element structures and stability under extension, Journal of Applied Mechanics 4 (1) (1995) 58–82.
[10] H. Kubler, Function of spiral grain in trees, Trees 5 (1991) 125–135.
[11] K. Schulgasser, A. Witztum, The mechanism of spiral grain formation in trees, Wood Science and Technology 41 (2007) 133–156.
[12] WWPA, Ponderosa Pine Species Facts, Western Wood Products Association, Oregon, 1995.
[13] K.S. Blonski, J.L. Schramel, Photo Series for Quantifying Natural Forest Residues: Southern Cascades, Northern Sierra Nevada, vol. 56 of General Technical Report, US Department of Agriculture, California, 1981.
[14] J. Belnap, D.A. Gillette, Disturbance of biological soil crusts: impacts on potential wind erodibility of sandy desert soils in southeastern utah, Land Degradation and Development 8 (12) (1997) 355–362.
[15] Forest-Product-Laboratory, Wood handbook – wood as an engineering material, General Technical Report, US Department of Agriculture, 1999.
[16] J. Bodig, B.A. Jayne, Mechanics of Woods and Wood Composites, Van Nostrand Reinhold, New York, 1982.